The effect of nanostructure dimensionality on the photoelectrochemical properties of derived TiO_2 films

Hye Won Jeong , Wu Haihua , Gergely F. Samu , Paul Rouster , István Szilágyi , Hyunwoong Park , Csaba Janáky

PII: S0013-4686(21)00190-0
DOI: https://doi.org/10.1016/j.electacta.2021.137900
Reference: EA 137900

To appear in: *Electrochimica Acta*

Received date: 7 December 2020
Revised date: 28 January 2021
Accepted date: 29 January 2021

Please cite this article as: Hye Won Jeong , Wu Haihua , Gergely F. Samu , Paul Rouster , István Szilágyi , Hyunwoong Park , Csaba Janáky , The effect of nanostructure dimensionality on the photoelectrochemical properties of derived TiO_2 films, *Electrochimica Acta* (2021), doi: https://doi.org/10.1016/j.electacta.2021.137900

The effect of nanostructure dimensionality on the photoelectrochemical properties of derived TiO_2 films

Hye Won Jeong,[1,2] Wu Haihua,[1] Gergely F. Samu,[1] Paul Rouster,[3] István Szilágyi[1], Hyunwoong Park,[2] Csaba Janáky[1,*]

[1]Department of Physical Chemistry and Materials Science, Interdisciplinary Excellence Centre, University of Szeged, Aradi Square 1, Szeged, H-6720, Hungary

[2]School of Energy Engineering, Kyungpook National University, Daegu, 41566 Korea

[3]Institute of Condensed Matter and Nanosciences - Bio and Soft Matter, Université Catholique de Louvain, Louvain-la-Neuve, B-1348, Belgium

Abstract

Studying the effect of nanoscale morphology on the photoelectrochemical performance of semiconductor electrodes has been in the forefront of research for over a decade, there are still major inconsistencies and controversies in the literature. Here we aimed to resolve some of these issues, by the controlled preparation of TiO_2 photoelectrodes from nanoparticles, nanorods, and nanosheets, where the nano dimension of the 0D, 1D, and 2D structures was kept similar (about 10 nm). XRD, Raman spectroscopy, XPS and UPS were employed to confirm that the chemical nature of the nanostructures is nearly identical, they only differ in their morphology. Photoelectrodes were prepared keeping the loading amount, surface area, or the film thickness identical, to deconvolute all trivial effects, and only scrutinize the role of morphology. TiO_2 nanorod (NR) films exhibited the best photoelectrochemical performance in all comparisons, achieving ~4 mA cm^{-2} at 0.2 V vs. Ag/AgCl (under 100 mW cm^{-2}, Xe-lamp illumination). In stark contrast, TiO_2 nanosheet (NS) film showed the lowest performance owing to the small amount of active sites on the basal plane of the NSs and the insufficient charge carrier transport through the film. Overall, we have demonstrated that under carefully controlled conditions, it is possible to compare the PEC behavior of TiO_2 photoelectrodes, and that the 1D nanostructures outperformed its 0D and 2D counterparts.

1. Introduction

To efficiently utilize renewable energy and therefore reduce environmental pollution, there is a strong need for better solar-to-chemical energy conversion technologies. Among these, solar water splitting (using photoactive materials) has the capability of both storing energy and producing valuable chemicals [1-3]. Various materials are used in the studies focused on solar photoelectrochemical (PEC) hydrogen and chemical fuel production, such as metal oxides (TiO_2, Cu_xO, WO_3, etc.) [4, 5], sulfides [6], nitrides [7], and halides [8, 9]. In general, the low solar-to-chemical conversion efficiencies, however, still hamper the practical utilization of these materials and the process as a whole.

With the aim of rationally designing photo-electrocatalyst materials, it is worth summarizing the most important parameters, which affect the performance of a given photoelectrode. These are the bandgap energy, carrier density and mobility, crystallinity/preferred orientation, defects, surface area, particle dimension/morphology, intra- and inter particle electrical conductivity, surface groups (e.g., hydroxyl), hydrophilic/hydrophobic nature, and acid–base character [10]. The effects of these factors are complex and convoluted, for example, particle size can affect light absorption via size quantization effect; it can also influence light-scattering events, and dictate band bending as well. In this sense, therefore, optical, structural, and electronic factors are coupled. The nanoscale morphology can also impact surface roughness and hence influence adsorption of solution species. Grouping these factors into separate boxes can lead to the wrong conclusion that they exert their effects independently from each other. In fact, this study aims to unravel the role of nanoscale morphology by using systematically designed model materials to deconvolute some of the above effects as shown in what follows. Scheme 1. illustrates the complexity of these effects.

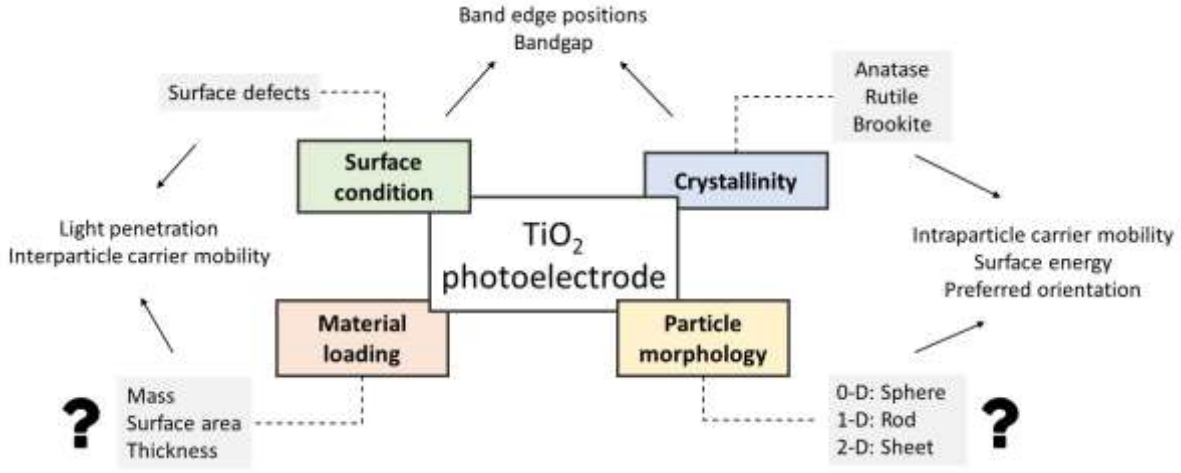

Scheme 1. Factors affecting the photoelectrochemical performance of TiO_2 electrodes.

The quantitative description of PEC processes is based on thick electrode films (with film thickness of over several micrometers) [11]. To enhance the current densities to a level which makes practical significance, however, photoelectrodes with large specific surface area are needed. This necessitates the use of nanostructured photoelectrodes, which is a well-studied but surprisingly qualitatively understood area. Photoexcitation generates carriers with finite mobility and lifetime. To efficiently drive solar-to-fuel conversion reactions, these carriers need to reach the photoelectrode interfaces at the electrolyte and at the back contact [12]. A recent review article (focused on water splitting, and mostly on water oxidation in particular) clearly highlighted the effect of nanostructures on carrier generation and collection, surface recombination, and on the size of space charge layers [13]. Its conclusions, however, were drawn from scattered studies, performed in different laboratories.

Interestingly, there is also a lack of information on morphological effects. There are pioneering studies on Si micro- [14, 15], and nanowires [16], where efficient charge carrier collection was demonstrated while maintaining sufficient light absorption. At the same time, there is no consensus whether there is an optimal morphology for PEC applications. Furthermore, there is no coherent information how the dimensionality of the photoelectrode material influences the PEC performance. Consequently, the synthesis of photoelectrode materials with controlled morphology is an attractive approach to

enhance solar-to-fuel conversion efficiency. An optimized morphology might provide enhanced light absorption, increased number of active surface sites, and fast charge transfer compared to systems that utilize planar architectures [17].

Materials chemistry provides various synthetic methods (such as hydrothermal, anodization, and electrodeposition) to achieve control over morphology [18-20]. TiO_2 is a suitable model material to test PEC water oxidation, as (1) it is chemically stable in aqueous solution, and (2) proper synthetic methods are available to prepare nanostructured morphologies (rod, plate, sphere, etc.) [21-23]. These differences in morphology generally also affect the existence of specific crystal phases and surface conditions [21, 24-26]. Specifically, depending on the shape of the photoelectrode materials, it is possible to selectively expose specific crystallographic facets that ultimately influences the PEC behavior [13, 27]. For example, the high surface energy (001) plane of anatase TiO_2 has higher activity in oxidative photocatalytic reactions, as opposed to the (101) plane, which is active in reduction reactions [28, 29]. There are various studies on the effect of the particle size and morphology-related factors for photocatalytic reactions [30-33], but systematic PEC studies are still lacking.

The PEC performance of different nanostructured TiO_2 films can only be meaningfully evaluated if they possess equivalent physical and chemical properties (such as crystallinity, particle size and material loading). In this regard, we synthesized different anatase TiO_2 nanostructures (nanoparticles, nanorods, and nanosheets) using hydrothermal synthesis. Subsequently, we fabricated photoanodes with controlled mass loading, thickness, and active surface area, respectively. We found that the TiO_2 nanorod (TiO_2 NR) photoelectrodes exhibit superiority, owing to enhanced charge carrier transport within the photoelectrode, and accelerated charge transfer from surface into the solution.

2. Experimental Section

2.1. Synthesis of TiO_2 nanostructures and film preparation

Scheme 2 shows the preparation procedure of nanostructured TiO_2 films via a two-step process. Different TiO_2 nanostructures (nanoparticles, nanorods, and nanosheets denoted

as TiO_2 NP, TiO_2 NR, TiO_2 NS) were prepared using the appropriate hydrothermal methods [22, 34, 35]. For TiO_2 NP, titanium isopropoxide (Aldrich, 97%), oleic acid (Alfa Aesar, 90%), and oleylamine (Aldrich, 70%) were used. Both TiO_2 NR and NS nanostructures were synthesized using titanium butoxide (Sigma Aldrich, 99 %). In these syntheses, hydrofluoric acid (VWR, 40 %) or ammonium hydroxide and hydrogen peroxide (VWR, 30 %) acted as supporting reagents, respectively. The details of each synthesis process are described in the *Supporting Information.* The as-prepared TiO_2 nanostructures were dispersed in ethanol (VWR, 95%) and sonicated for 1 hour to obtain well-dispersed suspensions. FTO glasses (surface resistivity ~ 7 Ω/sq) were ultrasonically cleaned with acetone, ethanol, and deionized water each for 15 min. Then the TiO_2 suspension was spray-coated on the FTO glass at 140 ℃, followed by annealing in air at 350 ℃ for 1 hour to obtain FTO/TiO_2 photoelectrodes.

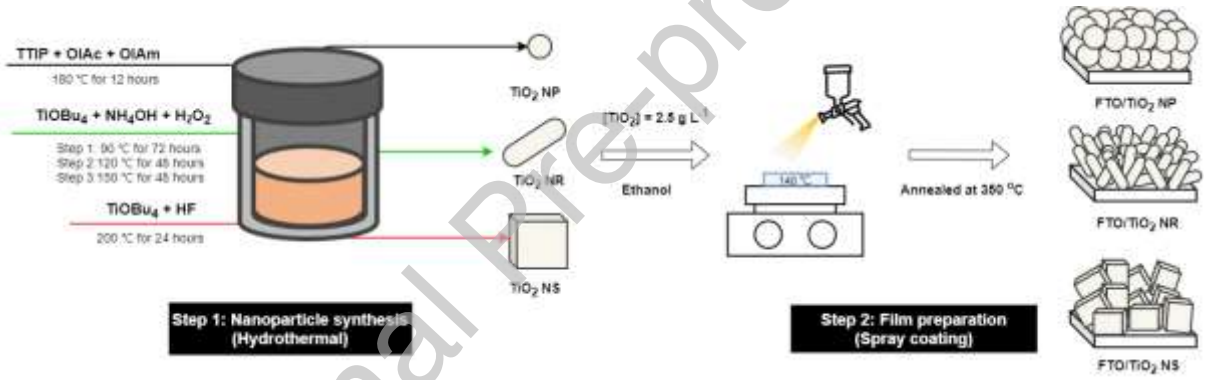

Scheme 2. The fabrication of nanostructured TiO_2 films on FTO glass substrate via two-step process.

2.2. Photoelectrode characterization

The morphology of the as-prepared nanoparticles was analyzed using transmission electron microscopy (TEM, FEI Tecnai G_2 20 X-Twin type) operating at an acceleration voltage of 200 kV and the size distribution of the samples was counted with ImageJ software. Field-emission scanning electron microscopy (FE-SEM, Hitachi S-4700) images (cross-section) provided the thickness of the as-prepared TiO_2 films. X-ray diffraction (XRD) patterns were measured with Rigaku Miniflex II instrument, operating with a Cu Kα, radiation source (λ = 0.1541 nm). Rietveld refinement was carried out using GSAS Ⅱ software on each pattern to identify the phase composition and crystallinity of each sample [36]. UV–vis absorption spectra were obtained with a Shimadzu UV-3600 Plus

spectrophotometer equipped with an integrating sphere. The optical bandgap energy of the films was determined by following the Tauc method [37]:

$$(\alpha h\nu)^n = (h\nu - E_g)$$

where α, $h\nu$ and E_g refer to the diffuse absorption coefficient, light energy, and optical bandgap energy and n = 0.5 for an indirect transition.

Raman spectra were measured on a Bruker SENTERRA 2 using 532 nm laser source (operating intensity ≤ 2.5 mW) with an x50 objective. X-ray photoelectron spectroscopy (Al Kα) was carried out with a SPECS instrument equipped with a PHOIBOS 150 MCD 9 hemispherical analyzer. The analyzer was used in fixed analyzer transmission mode with 40 eV pass energy for the survey scans and 20 eV pass energy for the high-resolution scans. Charge referencing was done to the adventitious carbon (284.8 eV) on the surface of the sample. For spectrum evaluation, CasaXPS commercial software package was used. Ultra-violet photoelectron spectroscopy (UPS) was performed with a He (I) excitation (21.2 eV) source. There was 5.0 V of external bias applied to the samples to accelerate secondary electrons to the analyzer. The work function (ϕ) was determined by the following equation: $\phi = h\nu - (E_{\mathrm{Cutoff}} - E_{\mathrm{F}})$, where hν is the photon energy (21.2 eV), E_{Cutoff} is the cutoff energy of secondary electrons, and E_{F} is the Fermi level.

2.3. Photoelectrochemical studies

PEC activity of TiO_2 films was tested using a three-electrode setup with a platinum plate and Ag/AgCl as a counter and a reference electrode, respectively. Linear sweep photovoltammograms were measured in 0.1 M sodium sulfite and sodium sulfate solutions using a UV-vis light source (HAMAMATSU-LC8, 100 mW cm^{-2}). All PEC data were recorded after Ar-purging the solution for 30 min to remove O_2 from the solution. Linear sweep voltammograms were obtained by sweeping the potential from –1.2 to 0.5 V *vs.* Ag/AgCl (3 M NaCl) at a scan rate of 2 mV s^{-1} under chopped illumination with a frequency of 0.1 Hz (Metrohm Autolab, PGSTAT204). The incident photon-to-current conversion efficiency (IPCE) was measured using a Newport Quantum Efficiency Measurement System (QEPVSI-b), using the following equation: IPCE (%) = (1240 × I_{ph}) × 100/(P_{light} × λ), where I_{ph}, P_{light}, and λ refer to the photocurrent density at 0.2 V *vs.*

Ag/AgCl, photon flux, and wavelength, respectively [38]. The absorbed photon-to-current conversion efficiency (APCE) values were calculated from IPCE values using the following equation: APCE (%) = IPCE (%)/absorptance, where absorptance is defined as the fraction of electron-hole pairs generated per incident photon flux [39]. Intensity-modulated photocurrent spectroscopy (IMPS) was carried out in the 20000 Hz to 0.1 Hz frequency range, using sinusoidal light intensity modulation and bias illumination from 365 nm LED, in 0.1 M sodium sulfate solution. The amplitude of the sinusoidal modulation was about 10% of the original intensity.

3. Results and discussion

3.1. Physical characterization

The composition of the precursor solutions and the presence of different supporting reagents controlled the specific growth direction (and aspect ratio) of the TiO_2 nanostructures (see respective TEM images in Figure 1a-f). From the size distribution histogram of TiO_2 NP (Figure S1), an average particle size of 7.9 ± 0.83 nm was estimated. For TiO_2 NRs 17.9 ± 2.86 nm (diameter) and 87.2 ± 12.95 nm (length) values were recorded. For TiO_2 NS, the thickness and length of samples were around 11.0 ± 2.56 nm and 81.0 ± 38.2 nm, respectively.

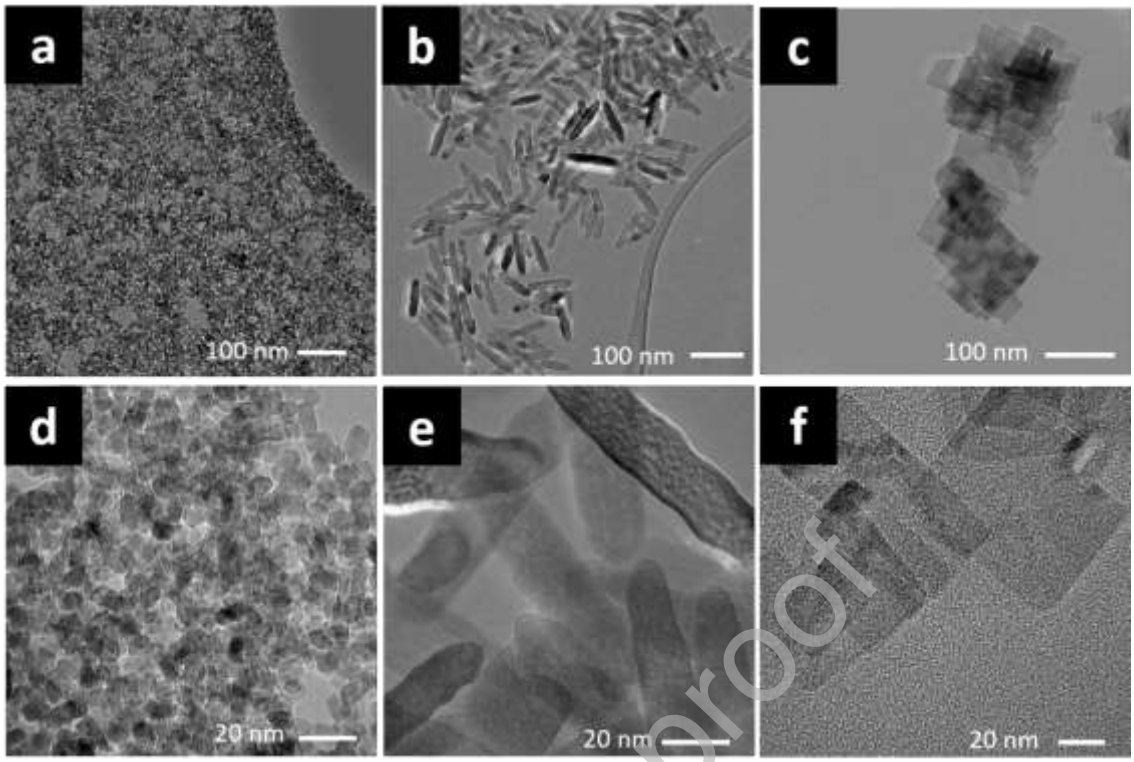

Figure 1. (a–c) TEM images of as-prepared TiO_2 NP, NR, and NS structures and (d–f) the respective high-resolution TEM images.

Top-down and cross-section FE-SEM images of TiO_2 films also confirmed that single particles kept their morphologies even after the film preparation and the annealing process (Figure 2). The thickness of TiO_2 NP, NR and NS film at 100 μg cm^{-2} was 338 nm, 537 nm and 952 nm, respectively.

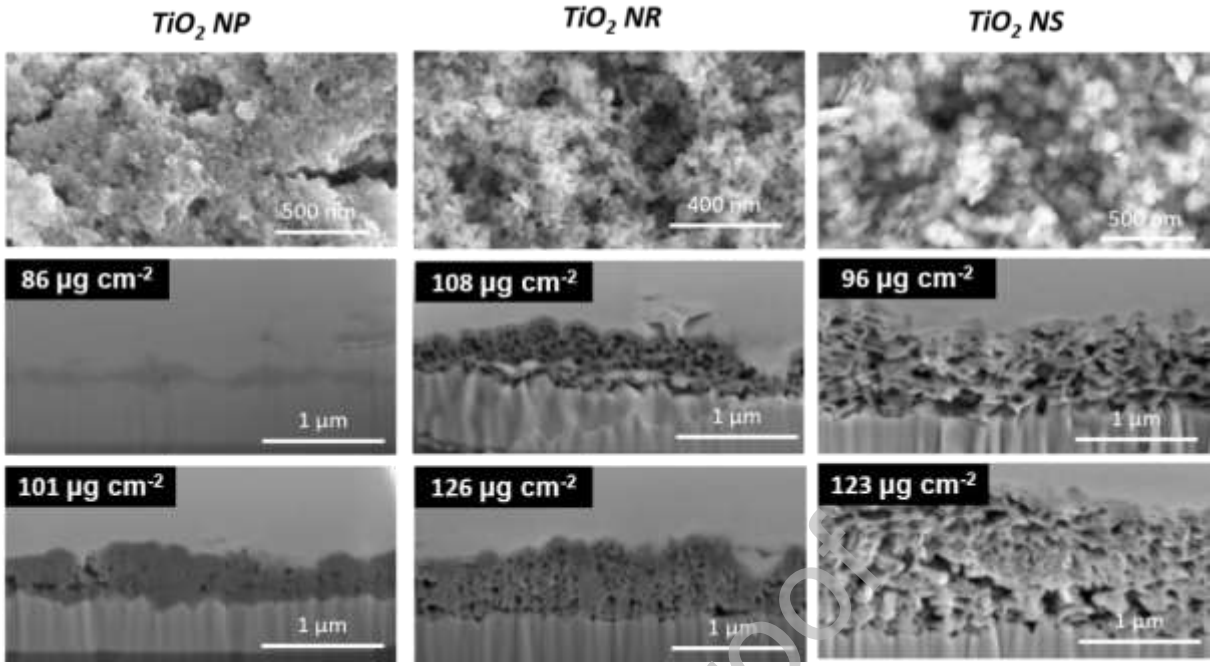

Figure 2**.** Top-down and cross-section SEM images of TiO_2 films.

The crystallinity of the nanostructured TiO_2 films was characterized using X-ray diffraction technique. Figure 3a presents the recorded diffraction patterns and their Rietveld refinement. The diffraction patterns could be indexed to the representative peaks of anatase TiO_2 (JCPDS #00-021-1272, *I41/amd*) confirming that phase purity was achieved for all samples [38, 40]. The same crystallographic planes are present in the different nanostructures, however, different peak broadenings were observed on the XRD patterns. From Rietveld refinement, the crystallographic domain size was extracted for the (101), (004) and (200) planes (Table S1). For TiO_2 NPs, all these planes contribute equally to the crystallographic domain (i.e., it consists of similar sized planes). For the TiO_2 NRs the size of the (004) plane exceeds the other two. This shows that the growth direction of TiO_2 NR favors the (004) orientation, with a high aspect ratio between the (004)/(101) planes [41]. For TiO_2 NS, the presence of the (004) plane becomes less pronounced, while there is a slight increase in the contribution of the (002) plane to the composition of the crystallographic domain (compared to the TiO_2 NP). For the TiO_2 NS samples a low (004)/(101) ratio was found (seen in Figure 1f and 3a) that is different from preceding literature references [23, 24] for the hydrothermally synthesized TiO_2 NS.

The optical properties of the films were investigated by recording their UV–Vis absorbance spectra (Figure S2), which were then converted to Tauc plots (as described in the Experimental section) to determine the optical bandgap energies. In Figure 3b, bandgap values of 3.32 eV, 3.34 eV, and 3.28 eV were determined for TiO_2 NP, NR, and NS, respectively. These are in the range reported for anatase TiO_2 (3.2-3.4 eV) [42, 43], indicating no marked difference in the optical properties of the different nanostructures.

The surface composition of the TiO_2 electrodes was analyzed by X-ray photoelectron spectroscopy (XPS). Peaks originating from the TiO_2 and the FTO substrate were identified on the survey spectra, which confirmed that the washing process removed possible contamination from the synthesis mixture (see Figure S3). Note that the minimum detection limit of XPS is below 1 atomic % in general [44]. In Figure 3c the Ti 2p region consists of two separated peaks of Ti $2p_{1/2}$ and $2p_{3/2}$ centered at 464.4 eV and 458.7 eV, characteristic of Ti^{4+} in TiO_2 [38, 45]. There were no additional species necessary to resolve the spectra, therefore no significant amount of Ti^{3+} species are present in any of the samples. Despite XPS provides surface sensitive information of samples, in our case it can represent almost the whole region of TiO_2 films due to the small size of single particles (Figure S1) at least in one dimension. Figure 3d shows the Raman spectra of the different TiO_2 films. The center position of vibration modes of TiO_2 NP, NR and NS are located at 144, 394, 514, and 636 cm^{-1}, further confirming the formation of anatase TiO_2 after the annealing process without generating disorder on the surface [20, 41].

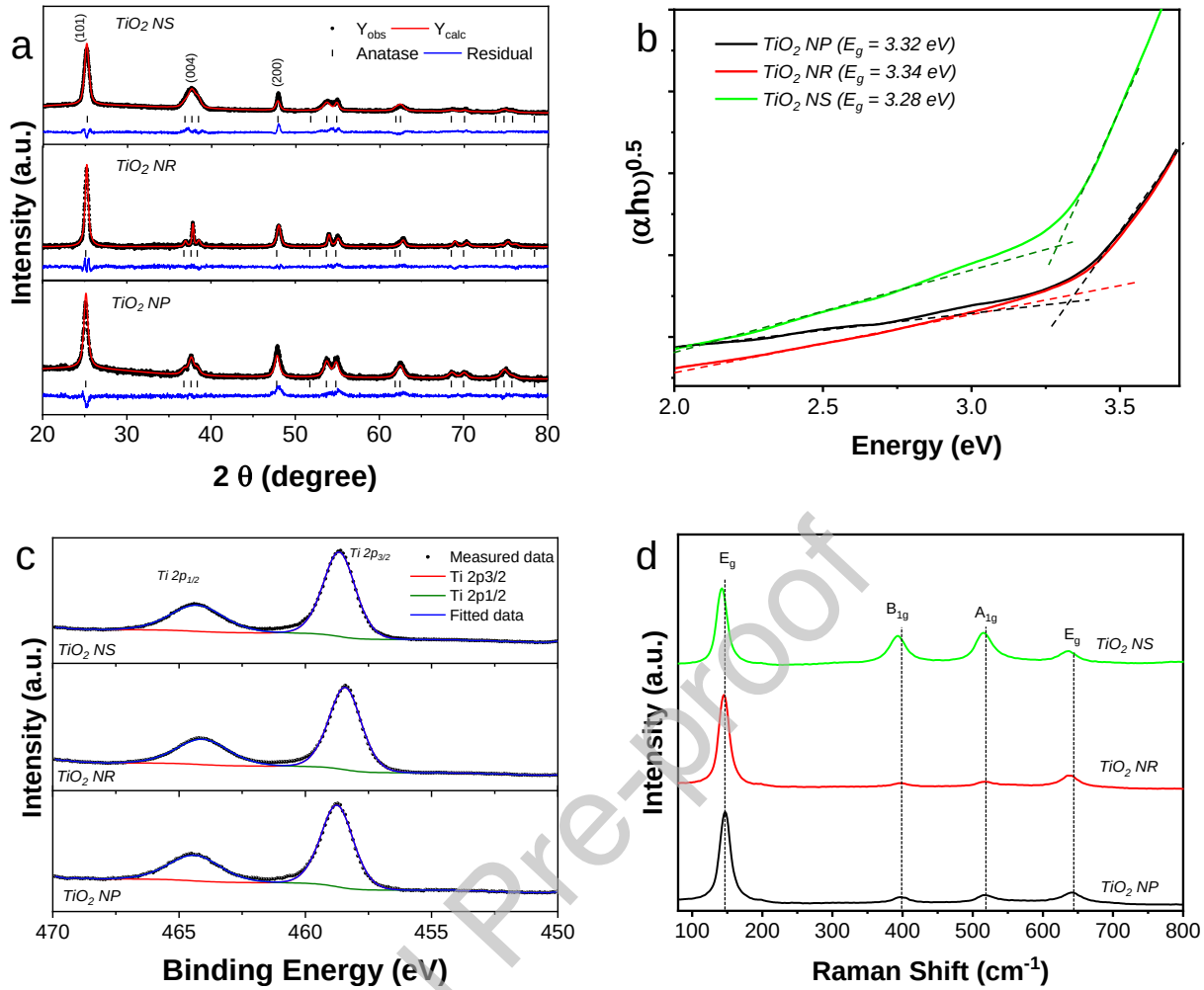

Figure 3. (a) Refined X-ray diffraction patterns and (b) optical bandgap energy estimation of TiO_2 films. Tauc plot is converted from absorption spectra, (c) XP spectra of Ti 2p region and (d) Raman spectra of TiO_2 NP, NR, and NS films.

Figure 4a shows the UP spectra of TiO_2 NP, NR, and NS respectively. In all cases the valence band spectra were deconvoluted into 5 components. The first state (I) at high binding energy corresponds to surface OH species (Figure S4) [46, 47]. The following three (II–IV) are the result of hybridized Ti 2p and O 2p orbitals, while the lowest binding energy state (V) corresponds to electron density within the bandgap (i.e., due to midgap states). In all TiO_2 structures, the edge of state IV determines the position of the valence band maximum (E_{VBM}), which matches well with literature values. The absence of the Ti^{3+} related contribution (that is usually located 0.7 eV below the conduction band edge) [48] further proves that there is no sign of Ti^{3+} in any of our samples. Notably, the distribution of the electron population within the valence band is

influenced by the shape (distribution of the different planes) of the TiO_2 nanostructures. Another important feature is the overall electron density within the bandgap (state V). These surface states can act as recombination centers during PEC processes. A higher density was observed for TiO_2 NSs and NPs compared to NRs, which might lead to increased surface recombination in the case of these nanostructures. Using the previously determined optical bandgap and the E_{VBM} values (Figure 4b), the band diagrams of the different TiO_2 nanostructures were constructed. Considering the VB positions alone, one could expect that TiO_2 NPs will show the best PEC oxidation performance, as they have a greater thermodynamic driving force for the water oxidation reactions.

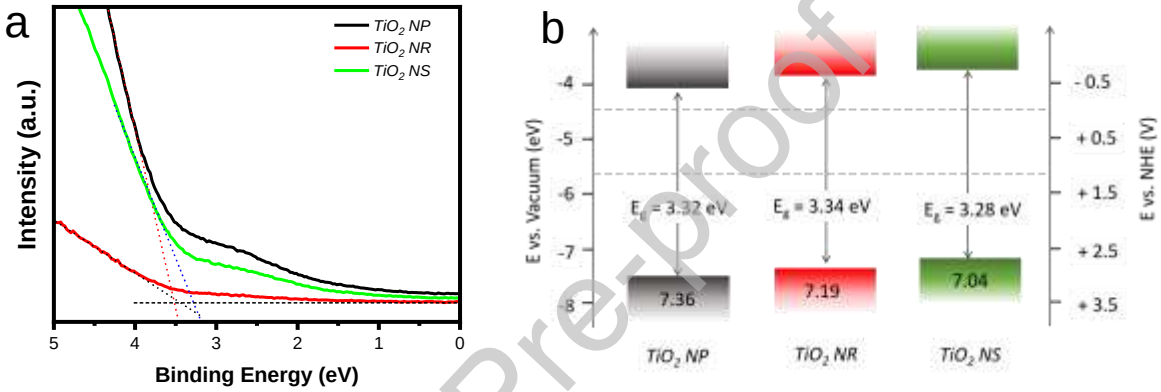

Figure 4. (a) UP spectra of TiO_2 films (b) band diagram estimated from parameters determined from UPS and UV-vis measurements.

Based on the various surface characterization techniques we conclude that the synthesized TiO_2 NP, NR, and NS structures possess similar size in at least one dimension and have similar surface composition. There was also no sign of doping elements (from the different precursors used), that could affect their PEC performance. Therefore, we can assume that the differences in PEC activity are predominantly rooted in their morphology and film fabrication conditions (electrode loading, surface area, and thickness), as discussed in what follows.

3.2. Photoelectrochemical activity of TiO_2 nanostructures

The PEC activity of anatase TiO_2 films with different morphology was evaluated through the systematic variation of the electrode properties (i.e., mass loading, thickness, active surface area). These measurements were conducted in a Na_2SO_3 electrolyte (hole

scavenger), which is widely applied for the comparison of PEC activities to avoid external limitations to the photocurrent (e.g., extensive surface recombination losses, sluggish reaction kinetics) [49, 50]. The initial comparison of the measured photocurrents for the different TiO_2 nanostructures was performed on the basis of different loadings between 60 and 120 µg cm^{-2} (Figure S5). The onset potential, where the photocurrents start to develop, was around − 0.9 V vs. Ag/AgCl for all samples, showing that the quasi-Fermi level is unaffected by the morphology of the nanostructures (see also UPS results). There is, however, a difference between the potential where the saturation photocurrent is reached for the different structures (0.0 V, − 0.1 V and − 0.2 V for TiO_2 NP, NR, and NS, respectively). Among the different nanostructures the highest photocurrent (~4.5 mA cm^{-2}) was obtained for TiO_2 NRs. Furthermore, the magnitude of the photocurrent varies differently for each nanostructure when the loading amount is increased. The photocurrent for TiO_2 NRs was more sensitive to the variation in mass loading, compared to the other nanostructures. Under low loading condition (60 µg cm^{-2}), TiO_2 NP and NS generate comparable photocurrent, while TiO_2 NR show less photocurrent than others (Figure 5a). At higher loadings (120 µg cm^{-2}), however, the maximum photocurrent of TiO_2 NR film increased to ~ 4 mA cm^{-2} at 0.2 V vs. Ag/AgCl, while TiO_2 NP and NS films performed similar to their low loading counterparts (Figure 5b). The insensitivity of the photocurrent to the mass loading suggests that (i) the active surface area of the photoelectrodes is not proportional with loading, or (ii) the charge carrier transport/collection through the TiO_2 NP and NS films is hindered.

To take the actual surface area of the samples into account, we determined the active surface area (ASA) for each nanostructure (see details in Supporting Information). Figure 5c shows the photocurrent of TiO_2 nanostructures measured with the same ASA (200 cm^2/ 1 cm^2 electrode area). At more negative potentials, TiO_2 NS film exhibit slightly higher photocurrent compared to TiO_2 NPs and NRs, while in the less negative region, TiO_2 NR films massively outperform the other two nanostructures. The comparison of the ASA and mass loading together with the photocurrent values provides further interesting information about these systems (Figure S6). It seems that increasing the ASA of TiO_2 NPs (three times) and NSs (two times) doesn't automatically yield proportional increases

in the observed photocurrents for these samples. This relationship exists, however, for the TiO_2 NR samples. Thus, in the case of NPs and NSs there are additional limitations to the performance, because the PEC reaction is not surface area-limited. The other phenomena that can affect the PEC performance is the charge extraction through the TiO_2 layers. The efficiency of this process can be negatively influenced by sluggish interparticle charge transfer [51]. As the orientation of the nanostructures is random in the films this can significantly decrease the measured photocurrent. In the case of TiO_2 NPs we expect the conduction mechanism to involve many interparticle interfaces (an intermediate photocurrent is observed). From the recorded photocurrent response, an inferior behavior can be observed in the case of TiO_2 NSs. This signals that a similar conduction mechanism is in play in this case involving many interparticle interfaces. In stark contrast the photocurrent of the TiO_2 NRs outperforms its counterparts signaling that intraparticle charge transfer is mostly involved in the conduction mechanism. We measured the thickness of TiO_2 films (with the same mass loading of 100 μg cm^{-2}) from the cross-section images of FE-SEM (Figure 2) and calculated the film density to evaluate the effect of thickness on the PEC performance. There was no clear trend between the layer density and the recorded photocurrent values (Figure 5d). The conclusion remained: the TiO_2 NR electrodes still outperformed its counterparts.

We performed similar experiments in sulfate-containing electrolyte (Figure S7). Under these conditions the predominant reaction is water oxidation, which is kinetically more sluggish than sulfite oxidation, thus surface recombination will have more time to prevail. The PEC performance of NPs and NSs, that have surface states present and have the least amount of exposed (001) facets, completely diminished. On the contrary, the TiO_2 NR retained most of its PEC activity. This priority is generally expected, considering the high photoreactivity of (001) fact with high portion of undercoordinated Ti atoms, and its preference to react with water [52, 53]. Furthermore, TiO_2 NRs have more surface hydroxyl groups (deduced from XPS and UP spectra).

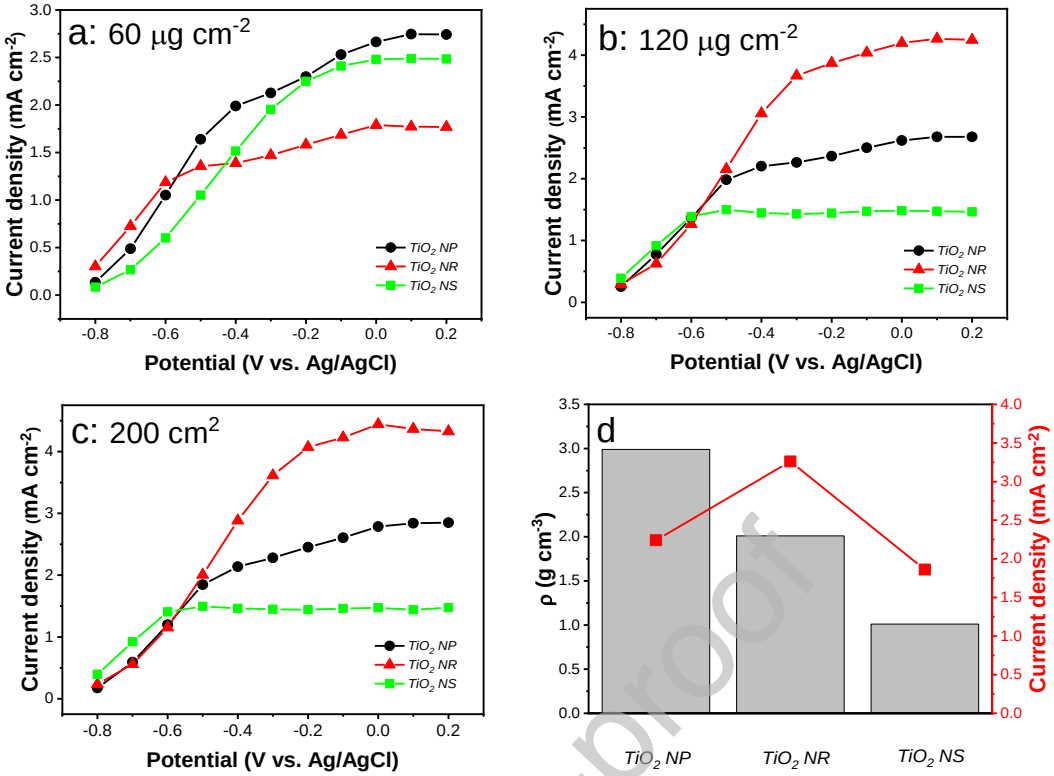

Figure 5. Photocurrent density as a function of potential for TiO_2 NP, NR, and NS films collected from linear sweep photovoltammograms in 0.1 M Na_2SO_3 under UV-vis light (100 mW cm^{-2}) illumination: (a) electrode loading of 60 μg cm^{-2}, (b) electrode loading of 120 μg cm^{-2} (c) active surface area of 200 cm^2. (d) The relationship between film density and the photocurrent density for the different nanostructures with an electrode loading of 100 μg cm^{-2}.

To further study the reasons behind the different PEC activity for the electrodes with various morphologies, IPCE curves were recorded for sulfite oxidation (i.e., sacrificial electron donor is present) and water oxidation. The NR samples utilize the higher energy portion of the UV spectrum more efficiently (with a maximum IPCE value obtained at 300 nm of ~40 %), compared to the NPs and NSs. The cut-off of the IPCE spectra mirrors that of the UV-vis absorbance spectra (Figure S2). The differences are even more striking in sulfate containing electrolyte: TiO_2 NR demonstrated the best efficiency, achieving a difference around three times compared to its TiO_2 NP and NS counterparts. We also recorded APCE curves of the samples (Figure S8) to remove losses from light scattering events in the layer. When these phenomena are removed, we can assess the losses that are related to charge carrier recombination caused by both transport and transfer issues

(from/to the surface of the electrode). From these results, TiO_2 NR still emerged victorious in the short wavelength regime, and it appears that the previously described issues are the factors underpinning the efficiency of the NP and NS samples.

As discussed previously, in Na_2SO_3 media the photocurrent yield will be unaffected by the charge carrier transfer from TiO_2 to the solution because of the fast kinetics of the redox reaction. As seen in the case of water oxidation, the slow kinetics of charge transfer decreases the photocurrents notably. From these two cases, we calculated the charge injection efficiency (η_{inj}) from the electrode to the species in the electrolyte from the ratio of the photocurrent densities of water and sulfite oxidation [54]:

$$\eta_{inj} = I_{\mathrm{ph}}^{\mathrm{H_2O}} / I_{\mathrm{ph}}^{\mathrm{sulfite}} \quad (1)$$

The potential dependence of η_{inj} is shown in Figure 6b for the different TiO_2 films prepared with similar loadings (~100 µg cm^{-2}). Strikingly, the photoelectrodes prepared from TiO_2 NS display very low η_{inj} (~2 %), which indicates that water oxidation is almost fully restricted on its surface. A slightly better injection efficiency was determined for TiO_2 NPs (~10 %), which was interestingly unaffected by the applied potential. In contrast the TiO_2 NR films showed increasing charge injection efficiency with increasing applied bias, reaching a ~35% at 0.0 V vs. Ag/AgCl. This increased injection efficiency of TiO_2 NR films in PEC water oxidation is caused by its larger extent of exposed (001) facet than others [55]. By increasing the potential more holes can reach the surface either caused by suppressed bulk recombination or by the better charge extraction in these samples [54].

To directly monitor the charge carrier dynamics in the prepared TiO_2 photoelectrodes we carried out IMPS measurements at different potentials. A representative IMPS spectrum is shown in Figure 6c (for TiO_2 NR electrode measured in 0.1 M Na_2SO_4 solution at − 0.1 V vs. Ag/AgCl). Two semicircles can be observed in the 4th and 1st quadrant, which is the typical behavior of n-type semiconductors. The semicircle in the 4th quadrant represents the RC time constant of the PEC process, which is associated with accumulation of holes on the surface, while the semicircle in the 1st quadrant carries information on the balance between surface recombination (k_{sr}) and charge transfer (k_{tr}) kinetics. From the semicircle

in the 1st quadrant the kinetic rate constants can be determined, which can be used to calculate the relative transfer efficiency (η_{tr}), represented by Equation 2 [56].

$$\eta_{tr} = \frac{k_{tr}}{(k_{tr} + k_{sr})}$$

Figure 6d, shows the potential dependence of the η_{tr} of TiO_2 NP and NR films. Note that the calculation of η_{tr} for TiO_2 NS films was not possible due to the low photocurrents, and thus the complicated nature of IMPS curves, which also gives an evidence of unfavored water oxidation on the surface (Figure S9). For the TiO_2 NP and NR samples the η_{tr} reached ~80 % at 0.0 V vs. Ag/AgCl. Interestingly below − 0.1 V vs. Ag/AgCl, TiO_2 NP films show higher η_{tr} values than TiO_2 NRs. This tendency can be understood by individually evaluating the contributions of surface recombination and charge transfer kinetics (Figure S10). At potentials more negative than − 0.1 V vs. Ag/AgCl the surface recombination rate constant for TiO_2 NR films was ~6-times greater than for TiO_2 NP films. As the potential increased, more charge carriers could be separated, and the recombination could be effectively suppressed in these films (see also charge injection efficiency data). Moreover, from the transient photocurrent profiles (Figure S7 inset), this distinct charge transfer difference was also observed. Note that the relative transfer efficiency does not take the efficiency of charge separation and charge collection into account, thus similar data could be obtained for the TiO_2 NPs, however, their performance in PEC water oxidation lags behind of TiO_2 NRs.

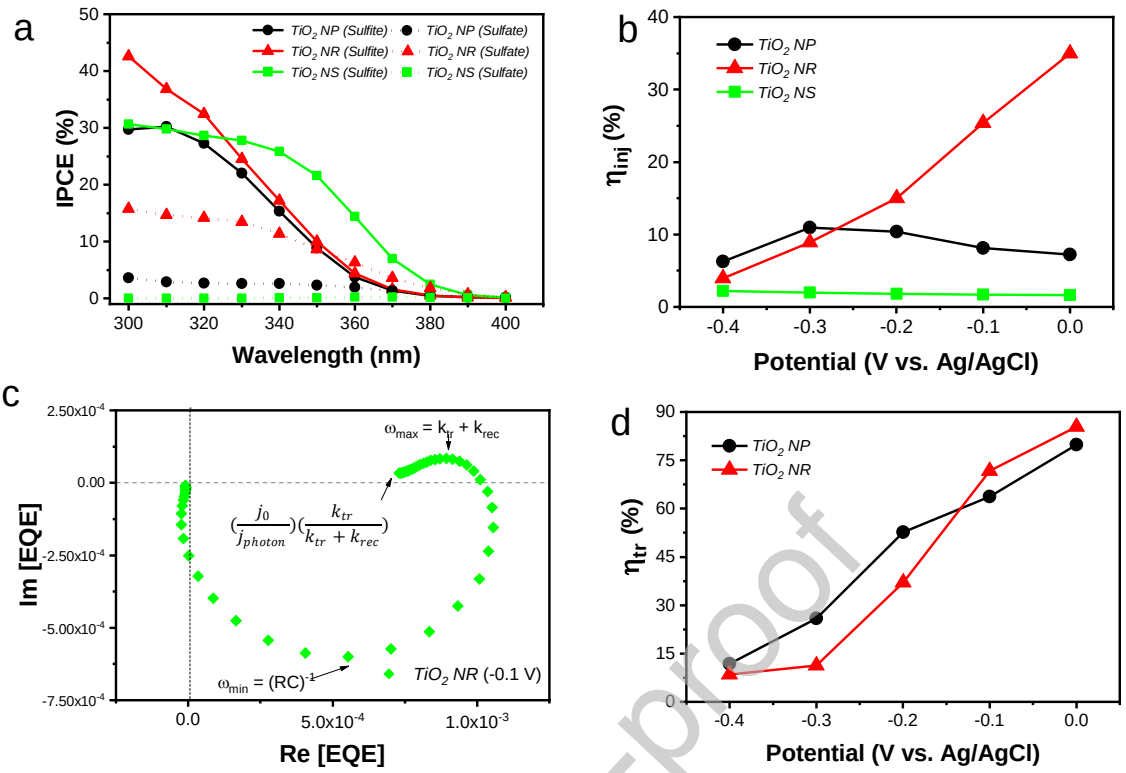

Figure 6. (a) IPCE profiles measured at 0.2 V vs. Ag/AgCl in different electrolytes for the various nanostructures, (b) charge transfer efficiency values derived from the measured photocurrent density in 0.1 M Na_2SO_3 and Na_2SO_4 electrolytes. (c) Representative IMPS spectra of TiO_2 NR films with an applied bias of − 0.1 V vs. Ag/AgCl in 0.1 M Na_2SO_4, and (d) the determined charge transfer efficiency as a function of applied potential for TiO_2 NP and NR samples. The TiO_2 loading of the electrodes was around 100 µg cm^{-2} in all cases.

4. Conclusions

We successfully synthetized anatase TiO_2 nanostructures, with different morphologies by hydrothermal methods. We tailored the number of dimensions that are in the nano-domain to prepare 0D (nanoparticles), 1D (nanorods), 2D (nanosheets) structures, while the size of the nanoscale domain remained similar (~10 nm). UV–vis spectroscopy and UPS measurements confirmed that the samples have similar optical properties. In a subsequent step, we prepared photoelectrodes from these structures by spray-coating. The effect of various film parameters (mass loading, active surface area, film density) on

the PEC performance of the photoelectrodes was carefully evaluated. Among these photoelectrodes, TiO_2 NR films exhibited superiority both in PEC sulfite and water oxidation in all comparisons. This enhanced PEC behavior of TiO_2 NR film was attributed to enhanced charge carrier transport in the film, smaller recombination rates and the facile charge transfer through its (001) plane, demonstrated by the results from IMPS and charge injection efficiency calculations. Although we tried to deconvolute all other effects apart from the morphology, there are fine differences behind the apparent similarity in their optical properties. The two most important are the decreased amount of surface states present in the case of NRs, and the distribution of the electron population within the valence band, which can also contribute to the enhanced performance.

Finally, we note that the thickness and length can be important parameters in determining the PEC performance of the TiO_2 nanostructures. Our goal was not to find the optimal particle dimensions, but to make a fair comparison among the 0D, 1D and 2D morphologies, under controlled conditions (in terms of electrode preparation as well). According to literature reports, the PEC activity of TiO_2 nanorods increased with nanorod length up to 1.38 μm. [56] In this study, however, the electrochemical surface area has not been taken into account, although it is a vital parameter. In the case of ultrathin 2D TiO_2, some studies showed superior photocatalytic HER performance, compared to its thicker counterparts. [57] Finding the optimal dimensions can be the subject of follow-up studies, under similarly rigorous conditions as presented in this manuscript.

Credit Author Statement

Hye Won Jeong: Methodology, Data Curation, Writing - Original Draft Investigation **Wu Haihua:** Investigation, Data Curation **Gergely F. Samu:** Methodology, Investigation, Writing - Original Draft **Paul Rouster:** Investigation **István Szilágyi:** Writing - Review & Editing **Hyunwoong Park:** Writing - Review & Editing **Csaba Janáky:** Conceptualization, Writing - Review & Editing, Supervision

Declaration_of_interest

The Authors have no competing interest.

Appendix. Supplementary materials

Experimental methods, TEM and SEM images, XRD analysis, and additional electrochemical measurements are discussed.

Corresponding Author

*janaky@chem.u-szeged.hu, twitter: @JanakyLab

Notes

The authors declare no competing financial interests.

Acknowledgments

This project has received funding from the European Research Council (ERC) under the European Union's Horizon 2020 research and innovation programme (grant agreement No 716539). This research was partially supported by the "Széchenyi 2020" program in the framework of GINOP-2.3.2-15-2016-00013 "Intelligent materials based on functional surfaces – from syntheses to applications" project. Dr. Hye Won Jeong is grateful to Basic Science Research Program through the National Research Foundation of Korea (NRF) (2019R1A6A3A12031559). The authors thank Dr. Bíborka Janáky-Bohner for her help with the manuscript preparation.

References

[1] U. Kang, S.K. Choi, D.J. Ham, S.M. Ji, W. Choi, D.S. Han, A. Abdel-Wahab, H. Park, Photosynthesis of Formate from CO_2 and Water at 1% Energy Efficiency via Copper Iron Oxide Catalysis, Energy & Environmental Science, 8 (2015) 2638-2643.

[2] E. Kecsenovity, B. Endrődi, P.S. Tóth, Y. Zou, R.A.W. Dryfe, K. Rajeshwar, C. Janáky, Enhanced photoelectrochemical performance of cuprous oxide/graphene nanohybrids, Journal of the American Chemical Society, 139 (2017) 6682-6692.

[3] D. Mersch, C.-Y. Lee, J.Z. Zhang, K. Brinkert, J.C. Fontecilla-Camps, A.W. Rutherford, E. Reisner, Wiring of photosystem II to hydrogenase for photoelectrochemical water splitting, Journal of the American Chemical Society, 137 (2015) 8541-8549.
[4] A.M. Mohamed, S.A. Shaban, H.A. El Sayed, B.E. Alanadouli, N.K. Allam, Morphology–photoactivity relationship: WO_3 nanostructured films for solar hydrogen production, International Journal of Hydrogen Energy, 41 (2016) 866-872.
[5] A.K. Nayak, Y. Sohn, D. Pradhan, Facile green synthesis of $WO_3 \cdot H_2O$ nanoplates and WO_3 nanowires with enhanced photoelectrochemical performance, Crystal Growth & Design, 17 (2017) 4949-4957.
[6] F. Vaquero, R. Navarro, J. Fierro, Influence of the solvent on the structure, morphology and performance for H_2 evolution of CdS photocatalysts prepared by solvothermal method, Applied Catalysis B: Environmental, 203 (2017) 753-767.
[7] G. Hitoki, T. Takata, J.N. Kondo, M. Hara, H. Kobayashi, K. Domen, An oxynitride, TaON, as an efficient water oxidation photocatalyst under visible light irradiation ($\lambda \leq$ 500 nm), Chemical Communications, (2002) 1698-1699.
[8] C. Le Paven-Thivet, A. Ishikawa, A. Ziani, L. Le Gendre, M. Yoshida, J. Kubota, F. Tessier, K. Domen, Photoelectrochemical properties of crystalline perovskite lanthanum titanium oxynitride films under visible light, The Journal of Physical Chemistry C, 113 (2009) 6156-6162.
[9] Y.-F. Xu, M.-Z. Yang, B.-X. Chen, X.-D. Wang, H.-Y. Chen, D.-B. Kuang, C.-Y. Su, A $CsPbBr_3$ perovskite quantum dot/graphene oxide composite for photocatalytic CO_2 reduction, Journal of the American Chemical Society, 139 (2017) 5660-5663.
[10] K. Rajeshwar, A. Thomas, C. Janáky, Photocatalytic activity of inorganic semiconductor surfaces: myths, hype, and reality, The Journal of Physical Chemistry Letters, 6 (2015) 139-147.
[11] K. Rajeshwar, Electron transfer at semiconductor-electrolyte interfaces, Electron Transfer in Chemistry, (2001) 278-352.
[12] B. Endrődi, G. Bencsik, F. Darvas, R. Jones, K. Rajeshwar, C. Janáky, Continuous-flow electroreduction of carbon dioxide, Progress in Energy and Combustion Science, 62 (2017) 133-154.
[13] S. Wang, G. Liu, L. Wang, Crystal facet engineering of photoelectrodes for photoelectrochemical water splitting, Chemical Reviews, 119 (2019) 5192-5247.
[14] S.W. Boettcher, J.M. Spurgeon, M.C. Putnam, E.L. Warren, D.B. Turner-Evans, M.D. Kelzenberg, J.R. Maiolo, H.A. Atwater, N.S. Lewis, Energy-conversion properties of vapor-liquid-solid–grown silicon wire-array photocathodes, Science, 327 (2010) 185-187.

[15] E.L. Warren, H.A. Atwater, N.S. Lewis, Silicon microwire arrays for solar energy-conversion applications, The Journal of Physical Chemistry C, 118 (2014) 747-759.
[16] A.P. Goodey, S.M. Eichfeld, K.-K. Lew, J.M. Redwing, T.E. Mallouk, Silicon nanowire array photoelectrochemical cells, Journal of the American Chemical Society, 129 (2007) 12344-12345.
[17] J.H. Bang, P.V. Kamat, Solar cells by design: photoelectrochemistry of TiO_2 nanorod arrays decorated with CdSe, Advanced Functional Materials, 20 (2010) 1970-1976.
[18] H.W. Jeong, W.-S. Chae, B. Song, C.-H. Cho, S.-H. Baek, Y. Park, H. Park, Optical Resonance and Charge Transfer Behavior of Patterned WO_3 Microdisc Arrays, Energy & Environmental Science, 9 (2016) 3143-3150.
[19] J. Zhang, Z. Liu, Z. Liu, Novel WO_3/Sb_2S_3 heterojunction photocatalyst based on WO_3 of different morphologies for enhanced efficiency in photoelectrochemical water splitting, ACS Applied Materials & Interfaces, 8 (2016) 9684-9691.
[20] H. Cui, W. Zhao, C. Yang, H. Yin, T. Lin, Y. Shan, Y. Xie, H. Gu, F. Huang, Black TiO_2 nanotube arrays for high-efficiency photoelectrochemical water-splitting, Journal of Materials Chemistry A, 2 (2014) 8612-8616.
[21] J. Li, D. Xu, Tetragonal faceted-nanorods of anatase TiO_2 single crystals with a large percentage of active {100} facets, Chemical Communications, 46 (2010) 2301-2303.
[22] W.-Z. Li, F. Gao, Y. Li, E.D. Walter, J. Liu, C.H. Peden, Y. Wang, Nanocrystalline anatase titania-supported vanadia catalysts: facet-dependent structure of vanadia, The Journal of Physical Chemistry C, 119 (2015) 15094-15102.
[23] X.-L. Cheng, M. Hu, R. Huang, J.-S. Jiang, HF-free synthesis of anatase TiO_2 nanosheets with largely exposed and clean {001} facets and their enhanced rate performance as anodes of lithium-ion battery, ACS Applied Materials & Interfaces, 6 (2014) 19176-19183.
[24] X. Han, Q. Kuang, M. Jin, Z. Xie, L. Zheng, Synthesis of titania nanosheets with a high percentage of exposed (001) facets and related photocatalytic properties, Journal of the American Chemical Society, 131 (2009) 3152-3153.
[25] K. He, Q. Wen, C. Wang, B. Wang, S. Yu, C. Hao, K. Chen, Synthesis of Anatase TiO_2 with Exposed (100) Facets and Enhanced Electrorheological Activity, Soft Matter, 13 (2017) 7879-7889.
[26] W.-J. Ong, L.-L. Tan, S.-P. Chai, S.-T. Yong, A.R. Mohamed, Highly reactive {001} facets of TiO_2-based composites: synthesis, formation mechanism and characterization, Nanoscale, 6 (2014) 1946-2008.

[27] Y. Liu, D. Huang, H. Liu, T. Li, J. Wang, ZnO tetrakaidecahedrons with coexposed {001},{101}, and {100} facets: shape-selective synthesis and enhancing photocatalytic performance, Crystal Growth & Design, 19 (2019) 2758-2764.
[28] J. Yu, J. Low, W. Xiao, P. Zhou, M. Jaroniec, Enhanced photocatalytic CO_2-reduction activity of anatase TiO_2 by coexposed {001} and {101} facets, Journal of the American Chemical Society, 136 (2014) 8839-8842.
[29] T. Butburee, P. Kotchasarn, P. Hirunsit, Z. Sun, Q. Tang, P. Khemthong, W. Sangkhun, W. Thongsuwan, P. Kumnorkaew, H. Wang, K. Faungnawakij, New understanding of crystal control and facet selectivity of titanium dioxide ruling photocatalytic performance, Journal of Materials Chemistry A, 7 (2019) 8156-8166.
[30] N. Roy, Y. Park, Y. Sohn, K.T. Leung, D. Pradhan, Green synthesis of anatase TiO_2 nanocrystals with diverse shapes and their exposed facets-dependent photoredox activity, ACS Applied Materials & Interfaces, 6 (2014) 16498-16507.
[31] Á. Veres, J. Ménesi, C. Janáky, G.F. Samu, M.K. Scheyer, Q. Xu, F. Salahioglu, M.V. Garland, I. Dékány, Z. Zhong, New insights into the relationship between structure and photocatalytic properties of TiO_2 catalysts, RSC Advances, 5 (2015) 2421-2428.
[32] A. McLaren, T. Valdes-Solis, G. Li, S.C. Tsang, Shape and Size Effects of ZnO Nanocrystals on Photocatalytic Activity, Journal of the American Chemical Society, 131 (2009) 12540-12541.
[33] M. Farhadian, P. Sangpour, G. Hosseinzadeh, Morphology dependent photocatalytic activity of WO_3 nanostructures, Journal of Energy Chemistry, 24 (2015) 171-177.
[34] C.-T. Dinh, T.-D. Nguyen, F. Kleitz, T.-O. Do, Shape-controlled synthesis of highly crystalline titania nanocrystals, ACS Nano, 3 (2009) 3737-3743.
[35] P. Rouster, M. Pavlovic, I. Szilagyi, Improving the stability of titania nanosheets by functionalization with polyelectrolytes, RSC Advances, 6 (2016) 97322-97330.
[36] B.H. Toby, R.B. Von Dreele, GSAS-II: the genesis of a modern open-source all purpose crystallography software package, Journal of Applied Crystallography, 46 (2013) 544-549.
[37] D. Roy, G.F. Samu, M.K. Hossain, C. Janáky, K. Rajeshwar, On the measured optical bandgap values of inorganic oxide semiconductors for solar fuels generation, Catalysis Today, 300 (2018) 136-144.
[38] H.W. Jeong, K.J. Park, D.S. Han, H. Park, High efficiency solar chemical conversion using electrochemically disordered titania nanotube arrays transplanted onto transparent conductive oxide electrodes, Applied Catalysis B: Environmental, 226 (2018) 194-201.

[39] Z. Chen, T.F. Jaramillo, T.G. Deutsch, A. Kleiman-Shwarsctein, A.J. Forman, N. Gaillard, R. Garland, K. Takanabe, C. Heske, M.J.J.o.M.R. Sunkara, Accelerating materials development for photoelectrochemical hydrogen production: Standards for methods, definitions, and reporting protocols, Journal of Materials Research, 25 (2010) 3.
[40] H. Ding, S.S. Dwaraknath, L. Garten, P. Ndione, D. Ginley, K.A. Persson, Computational approach for epitaxial polymorph stabilization through substrate selection, ACS Applied Materials & Interfaces, 8 (2016) 13086-13093.
[41] F. Tian, Y. Zhang, J. Zhang, C. Pan, Raman spectroscopy: a new approach to measure the percentage of anatase TiO_2 exposed (001) facets, The Journal of Physical Chemistry C, 116 (2012) 7515-7519.
[42] T. Lana-Villarreal, Y. Mao, S.S. Wong, R. Gómez, Photoelectrochemical behaviour of anatase nanoporous films: effect of the nanoparticle organization, Nanoscale, 2 (2010) 1690-1698.
[43] K. Kiatkittipong, J. Scott, R. Amal, Hydrothermally synthesized titanate nanostructures: impact of heat treatment on particle characteristics and photocatalytic properties, ACS Applied Materials & Interfaces, 3 (2011) 3988-3996.
[44] A.G. Shard, Detection limits in XPS for more than 6000 binary systems using Al and Mg Kα X-rays, Surface and Interface Analysis, 46 (2014) 175-185.
[45] I.S. Cho, J. Choi, K. Zhang, S.J. Kim, M.J. Jeong, L. Cai, T. Park, X. Zheng, J.H. Park, Highly efficient solar water splitting from transferred TiO_2 nanotube arrays, Nano Letters, 15 (2015) 5709-5715.
[46] A. Orendorz, J. Wüsten, C. Ziegler, H. Gnaser, Photoelectron spectroscopy of nanocrystalline anatase TiO_2 films, Applied Surface Science, 252 (2005) 85-88.
[47] S.A. Chambers, T. Droubay, T.C. Kaspar, M. Gutowski, Experimental determination of valence band maxima for $SrTiO_3$, TiO_2, and SrO and the associated valence band offsets with Si (001), Journal of Vacuum Science & Technology B: Microelectronics and Nanometer Structures Processing, Measurement, and Phenomena, 22 (2004) 2205-2215.
[48] L. Fleming, C. Fulton, G. Lucovsky, J. Rowe, M. Ulrich, J. Lüning, Local bonding analysis of the valence and conduction band features of TiO_2, Journal of Applied Physics, 102 (2007) 033707.
[49] D. Kang, Y. Park, J.C. Hill, K.-S. Choi, Preparation of Bi-based ternary oxide photoanodes $BiVO_4$, Bi_2WO_6, and $Bi_2Mo_3O_{12}$ using dendritic Bi metal electrodes, The Journal of Physical Chemistry Letters, 5 (2014) 2994-2999.

[50] B. Gao, T. Wang, X. Fan, H. Gong, P. Li, Y. Feng, X. Huang, J. He, J. Ye, Enhanced water oxidation reaction kinetics on a $BiVO_4$ photoanode by surface modification with Ni_4O_4 cubane, Journal of Materials Chemistry A, 7 (2019) 278-288.
[51] F.E. Osterloh, Inorganic nanostructures for photoelectrochemical and photocatalytic water splitting, Chemical Society Reviews, 42 (2013) 2294-2320.
[52] J. Pan, G. Liu, G.Q. Lu, H.M. Cheng, On the true photoreactivity order of {001},{010}, and {101} facets of anatase TiO_2 crystals, Angewandte Chemie International Edition, 50 (2011) 2133-2137.
[53] A. Selloni, Anatase shows its reactive side, Nature Materials, 7 (2008) 613-615.
[54] S.K. Pilli, T.E. Furtak, L.D. Brown, T.G. Deutsch, J.A. Turner, A.M. Herring, Cobalt-phosphate (Co-Pi) catalyst modified Mo-doped $BiVO_4$ photoelectrodes for solar water oxidation, Energy & Environmental Science, 4 (2011) 5028-5034.
[55] L. Ye, J. Mao, J. Liu, Z. Jiang, T. Peng, L. Zan, Synthesis of anatase TiO_2 nanocrystals with {101},{001} or {010} single facets of 90% level exposure and liquid-phase photocatalytic reduction and oxidation activity orders, Journal of Materials Chemistry A, 1 (2013) 10532-10537.
[56] M. Rodriguez-Perez, I. Rodriguez-Gutierrez, A. Vega-Poot, R. Garcia-Rodriguez, G. Rodriguez-Gattorno, G. Oskam, Charge transfer and recombination kinetics at WO_3 for photoelectrochemical water oxidation, Electrochimica Acta, 258 (2017) 900-908.

Graphical abstract